

Research Article

Discharge and Optical Emission Spectrum Characteristics of a Coaxial Dielectric Barrier Discharge Plasma-Assisted Combustion Actuator

Pengfei Liu ^{1,2}, Liming He,^{2,3} and Bingbing Zhao³

¹Graduate School, Air Force Engineering University, Xi'an 710051, China

²Science and Technology on Plasma Dynamics Laboratory, Aeronautic Engineering College, Air Force Engineering University, Xi'an 710038, China

³Aeronautic Engineering College, Air Force Engineering University, Xi'an 710038, China

Correspondence should be addressed to Pengfei Liu; lpf_kgd@126.com

Received 14 March 2020; Revised 28 May 2020; Accepted 4 June 2020; Published 24 June 2020

Academic Editor: Mark Baker

Copyright © 2020 Pengfei Liu et al. This is an open access article distributed under the Creative Commons Attribution License, which permits unrestricted use, distribution, and reproduction in any medium, provided the original work is properly cited.

A coaxial dielectric barrier discharge plasma-assisted combustion actuator (DBD-PACA) system was set up to study its discharge and optical emission spectrum (OES) characteristics in space in this paper. Results showed that each discharge cycle can be divided into four stages: a, b, c, and d. Discharge-on only occurred in stages b and d. Comparatively, the discharge intensity was larger in stage d due to the memory effect of excited electrons. Moreover, Lissajous figure and current-voltage methods were utilized to calculate the power of the coaxial DBD-PACA, and both methods produced roughly similar results. The power presented an upward trend with increasing input voltage and airflow rate. In addition, numerous second positive system (SPS) excited nitrogen molecules were detected from the OES signals. The intensity of the spectral lines (297.54 nm, 315.76 nm, 336.96 nm, and 357.56 nm) first increased, then maintained, and then increased rapidly with the increased radius; however, the intensity of the spectral lines (380.34 nm, 405.80 nm, and 434.30 nm) basically remained unchanged, then increased, and finally decreased with the increased radius. The vibrational temperature first decreased quickly and then increased and reached the minimum at $r = 18$ mm with the increased radius. The vibrational temperatures at all collection points decreased with the increased input voltage. However, within the range of 0–280 L/min, when r was lower than 15 mm, the vibrational temperatures first increased rapidly and then decreased slowly; when r was greater than 15 mm, the vibrational temperatures first increased and then basically remained stable.

1. Introduction

Plasma, which is an equal density of negative and positive particles ionized gas, belongs to the fourth state of matter and is composed of charged particles (electrons and ions), atoms, radicals, molecules in ground and excited states, and photons [1, 2]. Plasma has been widely used in many fields, such as plasma-assisted combustion (PAC) [3], plasma surface modification [4], plasma sterilization [5], plasma active flow control [6], and plasma mutation breeding [7]. Among these, PAC is a remarkable solution to enlarging stable combustion boundary, improving combustion stability and combustion efficiency, and lowering nitric oxide

emissions; it addresses these issues at a low energy cost, as put forward and studied by numerous relevant experts [8–11]. The superior performance of the PAC actuator (PACA) is the key of PAC technology, and numerous plasma discharge devices, such as dielectric barrier discharge (DBD) [12–15], pulsed corona [16], microwave discharges [17], and gliding arc [18], were investigated to improve combustion. Retter et al. [19] designed a DBD actuator to enhance a hydrogen diffusion flame and studied the fundamental aspects of DBD plasmas such as the nonthermal self-limiting, and steamer was found with the presence of hydrogen. Mintousov et al. [20] studied the characteristics of the DBD actuator at high temperature and found that the percentage

of absorbed energy by DBD actuator grew with temperature and the energy input determined the gap inflow. Tang et al. [21] studied the effects of airflows on a multicathode DBD and found that the discharge intensity increased along the direction of airflow.

Since DBD plasma can produce heat, electrons, excited molecules, long-lifetime intermediate species, radicals, ions, ionic wind, and Lorentz force, it improves combustion mainly through three pathways: thermal, kinetic, and transport [22]. Depending on the Arrhenius law, plasma produces heat and then improves temperature to accelerate combustion chemical reactions in the thermal pathway. Plasma also produces active radicals via direct electron impact dissociation, ion impact and recombination dissociation, and collisional dissociations of reactants with electronically excited and vibrationally excited molecules to lower the energy barrier of combustion chemical reactions and shorten the combustion chemical reactions chains in the kinetic pathway. Plasma can break down the large fuel molecules and produce ionic changing the local flow field and facilitating flow turbulization and mixing of the reactants in the transport pathway. Although lots of efforts have been done on PAC, qualitative or even quantitative understanding of the three pathways has not been clear. Meanwhile, few of PACAs have been used to enhance combustion performance through injecting ionized airflows and gaseous fuel into combustor. The coaxial DBD-PACA we designed is used in this way, and its characteristics need to be studied before being installed in combustor.

The purpose of PAC is to consume little energy to achieve combustion improvement, so studying discharge characteristic of the PACA is essential, and the common diagnostic method is to obtain the voltage and current signals which can deduce current density, discharge pulse width, microdischarge, and so on. However, the breakdown and extinction voltages and the power consumption are more important discharge parameters for PACA applied to aero-engine combustor [23]. Breakdown and extinction voltages are used to evaluate the stable operating range of the PACA, and power consumption is used to evaluate the performance of the PACA. Therefore, the influences of input voltage and airflow rate on the breakdown and extinction voltages and power consumption were studied in this paper.

The optical emission spectrum (OES) is a common and effective method to diagnose the kinetic effect of PACA. Radiative transitions relative to OH, CN, H, N, O, N₂, C, and NO were identified in the PAC via the OES, and when the equivalence ratio increased from 0.4 to 1.4, the emissions respective to NO and C decreased, while the OH band intensity increased [10]. Lin et al. [24] applied the OES to study gliding arc plasma in gliding arc fuel injector and found that the significant thermal effect was caused by the arc column. To the best of the authors' knowledge, most researchers only study the spectra of a single point in the discharge area; thus, the results obtained were one-sided and incomplete. In this paper, the OES signals were captured at ten points with equal spacing along the radial direction of the coaxial DBD-PACA, and the results were more reliable and complete.

In the current study, a coaxial DBD-PACA experimental facility was established, and an oscilloscope was used to capture the discharge signals of the coaxial DBD-PACA. Meanwhile, a spectrograph was used to capture the OES signals of the plasma produced by the coaxial DBD-PACA. The major research focus of this work is to study the discharge and OES characteristics of the coaxial DBD-PACA and the effect of airflow rate and input voltage on the power calculated by Lissajous figure and current-voltage methods, analyze the spatial distribution of the spectrum, and obtain the trend of the vibrational temperature of the whole discharge area with increased airflow rate and input power.

2. Experimental Setup and Theory Analysis

2.1. Experimental Setup. Figure 1(a) shows a schematic of the experimental system. The experimental apparatus consisted of four primary parts: coaxial DBD-PACA, gas supply system, power supply, and measurement system. The inner electrode of coaxial DBD-PACA was a stainless steel tube with a 20 mm outer diameter and functioned in transporting gaseous fuel. The inner diameter of the quarter glass tube was 38 mm, whereas quarter glass thickness was 2 mm. The copper foil electrode adhered to the quarter glass tube and five layers of Kapton covering to prevent the glow discharge. For uniform discharge, the four parts of coaxial DBD-PACA should maintain concentricity, and the top view of the DBD-PACA is illustrated in Figure 1(b). In order to obtain homogeneous discharge plasma, a swirler was installed between the quartz glass tube and the inner electrode, and it was located at the upstream of the discharge area. Figures 1(c) and 1(d) show the discharge diagrams without and with swirler. The coaxial DBD-PACA was driven by an alternating current single high-voltage differential power (CTP-2000K), and this power supply was manufactured by Suman Electronics. The high-voltage end of the power supply was attached to the outer copper foil electrode and controlled by the voltage regulator, whereas the other end was connected to ground lead. The working frequency of the power supply was set to 9.5 kHz. The essence of the power supply is to increase the input voltage by thousands times to the applied voltage, and the applied voltage is controlled by the input voltage. The gas supply system mainly included a piston air compressor, and the flowmeter produced by Sevenstar was utilized to control the airflow rate flowing into the coaxial DBD-PACA.

The measurement system mainly consisted of a spectrograph, oscilloscope, and Canon digital signal lens reflex (DSLR) camera. The spectrograph (AvaSpec-ULS2048-4-USB2) produced by Avantes contained four channels to capture spectrum signals with the wavelength ranging from 200 nm to 950 nm and a slit width of 10 μm . The probe to collect the spectrum of the spectrograph was fixed on the slideway. And the spectra were collected at ten locations ($r = 10$ mm, 11 mm, 12 mm, 13 mm, 14 mm, 15 mm, 16 mm, 17 mm, 18 mm, and 19 mm), as shown in Figure 1(b). Tektronix P6015A (1000 : 1) high-voltage probe was used to measure the applied voltage of the coaxial DBD-PACA; Tektronix TPP1000 (10 : 1) low-voltage probe was used to

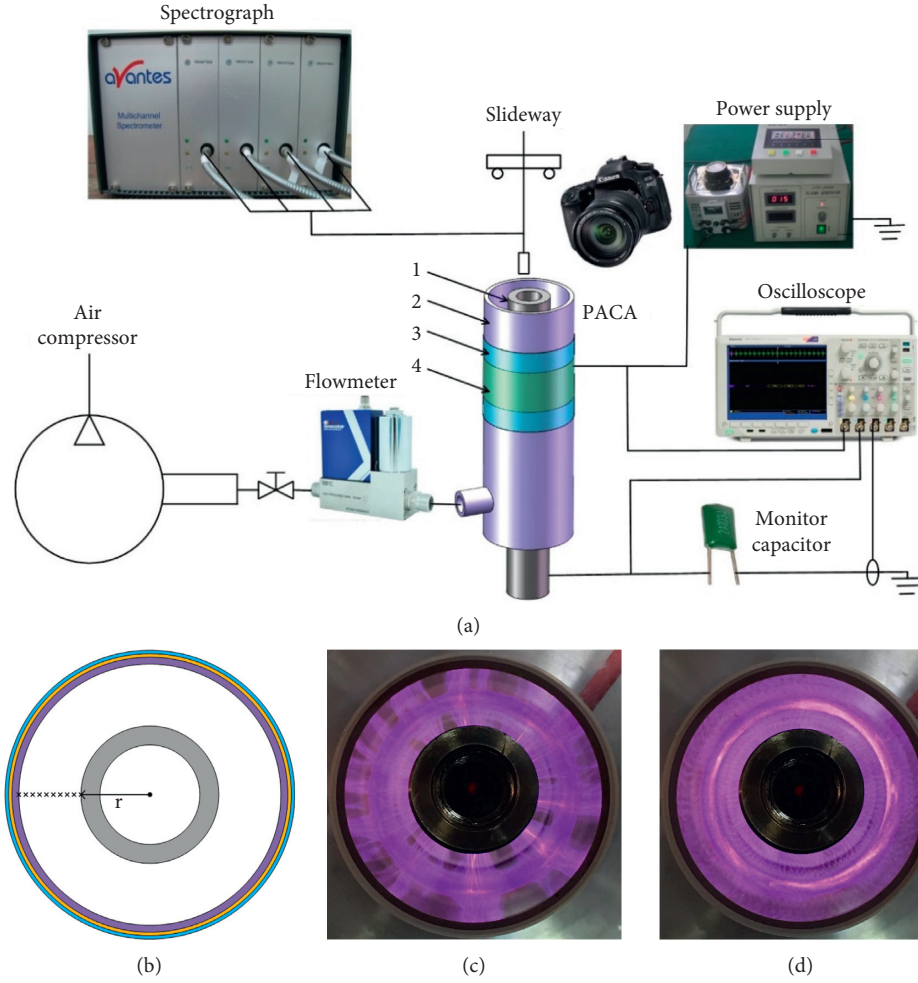


FIGURE 1: (a) Schematic of the experimental system, 1-inner electrode, 2-quartz glass tube, 3-copper foil electrode, and 4-five Kapton layers; (b) the top view of the coaxial DBD-PACA; (c) the discharge diagram without swirler; and (d) discharge diagram with swirler.

measure the applied voltage of the monitor capacitor; Tektronix TCP0030 current probe (1 : 1 for measurement at 5 A and 10 : 1 for measurement at 30 A; bandwidth, 120 MHz) was used to measure the current of the series circuit; all discharge signals were recorded by the oscilloscope (DPO4104B; Tektronix). Direct discharge plasma images were captured by a DSLR camera (Canon EOS 80D).

2.2. Power Measurement Methods. Two methods were used to calculate the power consumption of the coaxial DBD-PACA: Lissajous figure method and current-voltage method [25].

2.2.1. Lissajous Figure Method. The power was estimated through calculating the area of charge-voltage ($Q - V$) curve of the coaxial DBD-PACA. The key to this method was to connect a monitor capacitor (C_m) with a value much larger compared with the capacitance of the coaxial DBD-PACA without plasma discharge to the series circuit (Figure 2) [26]. And the value of C_m is 1000 pF in this experiment. Therefore,

the current passing through the monitor capacitor was computed as follows:

$$I_m(t) = \frac{dQ_m(t)}{dt}. \quad (1)$$

Instantaneous charge $Q_m(t)$ on the monitor capacitor was computed as follows:

$$Q_m(t) = C_m V_m(t). \quad (2)$$

The capacitance of the monitor capacitor was assumed to be constant over the applied voltage and frequency range of the coaxial DBD-PACA, thus obtaining the following:

$$I_m(t) = C_m \frac{dV_m(t)}{dt}. \quad (3)$$

As the current through the monitor capacitor must be identical to that passing through the coaxial DBD-PACA ($I_m(t) = I_{PACA}(t)$); the instantaneous power $P_{PACA}(t)$ dissipated by the coaxial DBD-PACA can be written as follows:

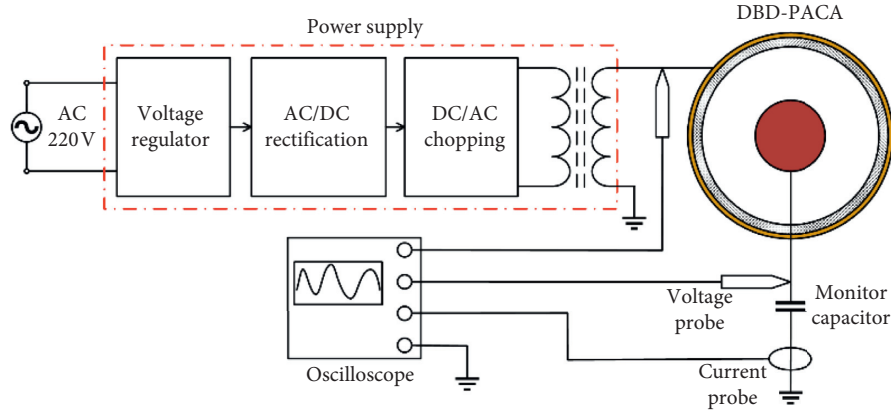


FIGURE 2: Electrical circuit diagrams of the DBD-PACA.

$$P_{\text{PACA}}(t) = V_{\text{PACA}}(t)I_{\text{PACA}}(t) = V_{\text{PACA}}(t)C_m \frac{dV_m(t)}{dt}. \quad (4)$$

So, the average power P over one discharge cycle period T was calculated with the following formula [27]:

$$\begin{aligned} P &= \frac{1}{T} \int_0^T P_{\text{PACA}}(t) dt = \frac{1}{T} \int_0^T V_{\text{PACA}}(t) C_m \frac{dV_m(t)}{dt} dt \\ &= \frac{1}{T} \int V_{\text{PACA}} C_m dV_m = \frac{1}{T} \oint_{\text{one cycle}} V_{\text{PACA}} dQ_m. \end{aligned} \quad (5)$$

Therefore, the instantaneous transport charge Q_m and the instantaneous applied voltage V_{PACA} plotted against each other generated a Lissajous curve in the Q_m - V_{PACA} plane. And the area inside the closed Lissajous curve divided by one discharge cycle period T was equal to the power of the coaxial DBD-PACA.

2.2.2. Current-Voltage Method. According to electrical properties, instantaneous power consumption can be calculated by multiplying the current-voltage signals on the coaxial DBD-PACA:

$$P_i = V_i I_i, \quad (6)$$

where V_i denoted the instantaneous applied voltage on the coaxial DBD-PACA, I_i represented the coaxial DBD-PACA instantaneous current, and P_i referred to the instantaneous power.

Current-voltage signals consist of numerous discontinuous points. Thus, the difference and summation method was introduced to the instantaneous power. The power was then computed as follows:

$$P = f \sum_{i=0}^N V_i I_i \Delta t, \quad (7)$$

where N specified the total signal points in one discharge cycle and Δt was the time interval between two adjacent signal points.

2.3. Vibrational Temperature Calculation Method. The particles in the excited vibrational state were easy to absorb the chemical reactants, which can overcome the reaction barrier, reduce the energy consumption, and promote the chemical reaction. The vibrational temperature described the intensity of molecular vibration excitation, which can be calculated by the multispectral line slope method. The spectral line intensity $I_{\nu',\nu''}$ of the vibration system of diatomic molecular emission spectrum was

$$I_{\nu',\nu''} = hc\nu_{\nu',\nu''} p_{\nu',\nu''} N_{\nu'}, \quad (8)$$

where ν' and ν'' represent the vibration quantum number of the upper and lower state, respectively, h was Planck's constant ($h = 6.62606975 \times 10^{-34}$ J.s), c was the speed of light, $\nu_{\nu',\nu''}$ was the emission spectral frequency, $p_{\nu',\nu''}$ was the transition probability between the upper and lower energy levels, and $N_{\nu'}$ was the molecular number of the upper state.

In the same electronic excited state, the number of molecules with different vibration-excited states was

$$N_{\nu'} = N_0 e^{-E_{\nu'}/kT_{\nu}}, \quad (9)$$

where N_0 indicated the number of the excited vibrational ground state in this electronic excited state, k was a constant ($k = 8.617689 \times 10^{-5}$ eV/K), and T_{ν} was the vibrational temperature.

According to spectroscopy, the vibrational energy $E_{\nu'}$ of the upper state can be expressed as follows:

$$E_{\nu'} = \omega_e \left(\nu' + \frac{1}{2} \right) - \omega_e x_e \left(\nu' + \frac{1}{2} \right)^2 + \omega_e y_e \left(\nu' + \frac{1}{2} \right)^3 - \dots, \quad (10)$$

where ω_e was the vibrational frequency of the harmonic oscillator, $\omega_e x_e$ was the first-order correction of the anharmonic vibration, and $\omega_e y_e$ was the second-order correction of the anharmonic vibration [28]. The following equation can be obtained by combining the above three equations:

$$\ln \frac{I_{\nu',\nu''}}{\nu_{\nu',\nu''} p_{\nu',\nu''}} = C - \frac{E_{\nu'}}{kT_{\nu}}, \quad (11)$$

Therefore, $\ln(I_{\nu',\nu''}/\nu_{\nu',\nu''} p_{\nu',\nu''})$ was a linear equation of the $(-E_{\nu'}/k)$, so the vibrational temperature of the plasma was the reciprocal of the slope of this equation. However, the fitting error exists in the vibrational temperature calculated by this method, and the error of spectral intensity also leads to the systematic error of vibrational temperature. In this paper, three groups of vibration-excited state bands, $\Delta\nu = -1$ (0-1, 1-2, 2-3), $\Delta\nu = -2$ (0-2, 1-3, 2-4), and $\Delta\nu = -3$ (0-3, 1-4, 2-5), were substituted into the above equation to calculate the vibrational temperature, respectively, and the average value was taken as the vibrational temperature of the plasma to reduce any discrepancies. Table 1 shows some spectral parameters of the SPS of nitrogen molecules used for calculating the vibrational temperature.

3. Results and Discussion

3.1. Discharge Characteristic. Figure 3 shows typical applied voltage, current, and charge waveforms with airflow rate of 200 L/min and input voltage of 130 V. Based on waveforms, the applied voltage and charge of the coaxial DBD-PACA discharge presented sinusoidal shapes, which were related to power supply characteristics. However, the current contained a series of intermittent high-amplitude spikes. The coaxial DBD-PACA discharge contained numerous filament channels (micro-discharge) with continuous formation and extinguishment, which resulted in the appearance of spikes [30]. The phase difference between the applied voltage and charge was approximated 6 μ s. Each discharge cycle can be roughly divided into four stages: a, b, c, and d. No spike (discharge-off) was observed in stages a and c. On the other hand, numerous spikes were noted in stages b and d, and the quantity and intensity were both considerably larger in stage d. The reason was attributed to the massive electrons attached to the quartz dielectric inner surface and formed a built-in electric field [31] with the direction opposite to the applied electric field in stage b, thus weakening the intensity of total electric field; however, both directions were same in stage d, thus strengthening the intensity of total electric field.

Figure 4 showed quarter discharge cycle waveform, which was the partial enlarged version of the waveforms in the green oval in Figure 3. The appearance of every spike caused a decrease in applied voltage across the coaxial DBD-PACA and increase in charge. When one discharge channel was broken down, resistance of the coaxial DBD-PACA decreased. However, the resistance of the monitor capacitor remained constant. Thus, the applied voltage across the coaxial DBD-PACA reduced. The circuit charge increased with increasing current. However, the number of spikes barely increased with increasing applied voltage amplitude.

Extinction and breakdown input voltages were essential characteristics of the coaxial DBD-PACA [32]. Figure 5 shows the extinction input voltage and breakdown input voltage versus the airflow rate. The data were the average of five experimental results under the same experimental conditions. The breakdown input voltage was notably greater than the extinction input voltage due to the energy of the coaxial DBD-PACA originated entirely from the power supply before breakdown of air; however, during the coaxial

TABLE 1: Parameters of the SPS ($N_2(C^3\Pi_u) \rightarrow N_2(B^3\Pi_g)$) of the nitrogen molecules [29].

$\nu' \rightarrow \nu''$	λ (nm)	$p_{\nu',\nu''}$ ($10^6 s^{-1}$)	$\nu_{\nu',\nu''}$ (10^{14} Hz)	$E_{\nu'}$ (cm^{-1})
0 \rightarrow 1	357.56	7.33	8.39	1013.28
1 \rightarrow 2	353.60	4.61	8.48	3014.22
2 \rightarrow 3	349.92	1.46	8.57	4981.08
0 \rightarrow 2	380.34	2.94	7.89	1013.28
1 \rightarrow 3	375.42	4.10	7.99	3014.22
2 \rightarrow 4	370.89	3.37	8.09	4981.08
0 \rightarrow 3	405.80	0.92	7.39	1013.28
1 \rightarrow 4	399.67	2.49	7.51	3014.22
2 \rightarrow 5	394.06	2.63	7.61	4981.08

DBD-PACA discharge, a low voltage was needed to maintain discharge under the action of electrons memory effect and built-in electric field. Moreover, the breakdown input voltage and extinction input voltage both increased with airflow rate as the aerodynamic force increased the relative minimum breakdown distance between two electrodes. Thus, a higher input voltage was needed to break down or maintain the microdischarge channels. The minimum extinction input voltage and breakdown input voltage reached 72.7 V and 77.0 V, respectively, in still air. The maximum extinction input voltage and breakdown input voltage measured 87.8 V and 91.0 V, respectively, when the airflow rate was 280 L/min.

Figure 6 shows the five cycles of Lissajous figures corresponding to the waveforms of the applied voltage and charge in Figure 3. Lissajous figures presented an almost-parallelogram shape, and the four edges represent the four stages of the coaxial DBD-PACA discharge. Stages a and c were in discharge-off state, but, stages b and d were in the state of discharge-on. Smooth Lissajous figures were obtained for stages a and c. However, Lissajous figures fluctuated in stages b and d, and fluctuation became more severe in stage d. When the coaxial DBD-PACA was discharging, negatively charged electrons were produced and moved along the direction of electric field, and wall charges appeared on the quarter dielectric inner side. When the applied voltage was positive, the electric field induced by wall charges was contrary to the external electric field, thus weakening the discharges. By contrast, when the applied voltage was negative, the direction of the electric field induced by wall charges was the same as that of the external electric field, thus strengthening the discharges.

The red loop was the average value of five cycles of Q_m - V_{PACA} Lissajous figures in Figure 6. In this study, to avoid systematic and experimental errors, the red loop was used as standard to calculate the area of Lissajous figure, which was used to obtain the power of the coaxial DBD-PACA.

Figure 7 shows the Lissajous figures and the power with the input voltage ranging from 90 V to 190 V at the condition of the airflow rate being 200 L/min. Figure 7(a) showed that the area of the Lissajous figure and maximum transport charge distinctly increased with increasing input voltage; however, the maximum applied voltage of the coaxial DBD-PACA increased slightly with increasing input voltage. So the input voltage has little effect on the maximum

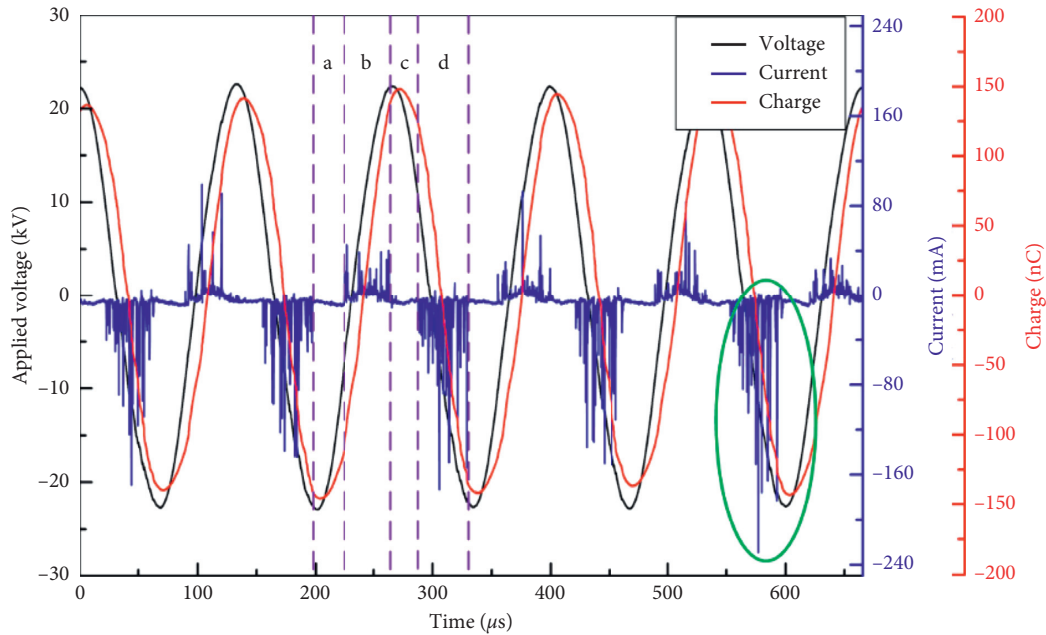


FIGURE 3: Typical voltage, current, and charge waveforms of the coaxial DBD-PACA.

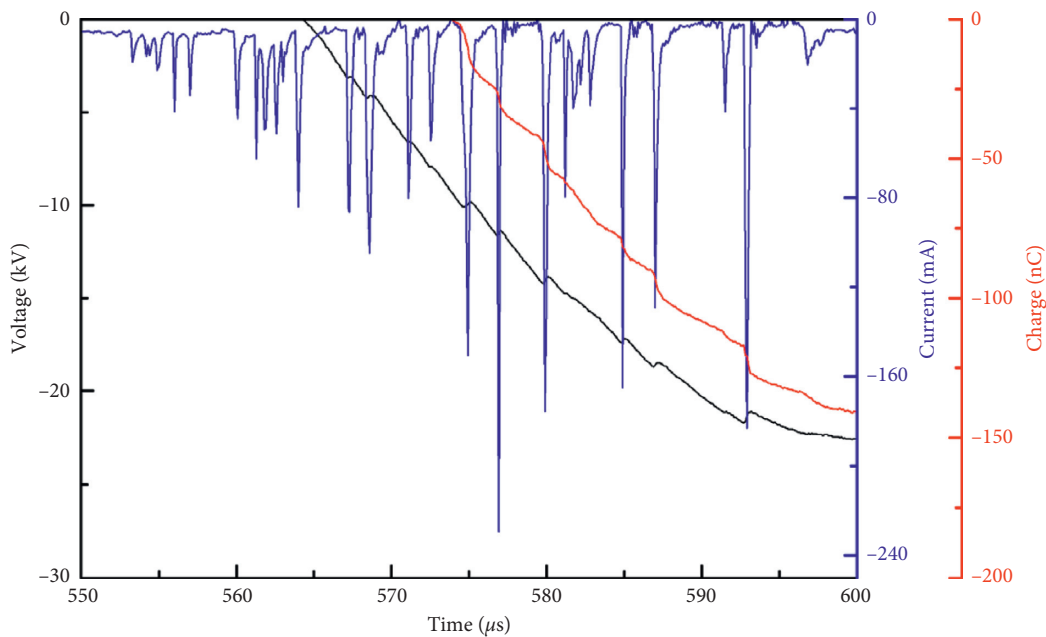


FIGURE 4: Part of the voltage, current, and charge waveforms of the coaxial DBD-PACA.

applied voltage, but the input voltage has a significant effect on the maximum transport charge. This phenomenon occurred as the current increased with increasing input voltage in the circuit; then more microdischarge channel breakdowns were observed in the coaxial DBD-PACA, and its equivalent resistance decreased. Thus, the assigned applied voltage of the monitor capacitor evidently increased. And depending on equation (2), the maximum transported charge also deservedly increased. Figure 7(b) demonstrated that the power calculated by Lissajous figures method and

current-voltage method both increased with increasing input voltage. The power calculated by the two methods presented differences caused by the theoretical errors.

Figure 8 shows the Lissajous figures and the power with the airflow rate from 0 L/min to 280 L/min at the condition of the input voltage being 130 V. Based on Figure 8(a), the area of the Lissajous figure fluctuated slightly with increasing airflow rate. As shown in Figure 8(b), the power followed a macroscopic upward trend along with fluctuation within a narrow range. The turbulence of airflow possibly caused the

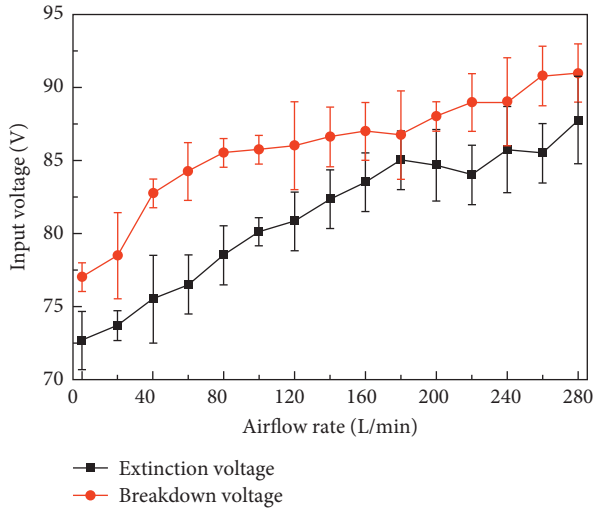


FIGURE 5: Breakdown and extinction discharge characteristics with the airflow rate.

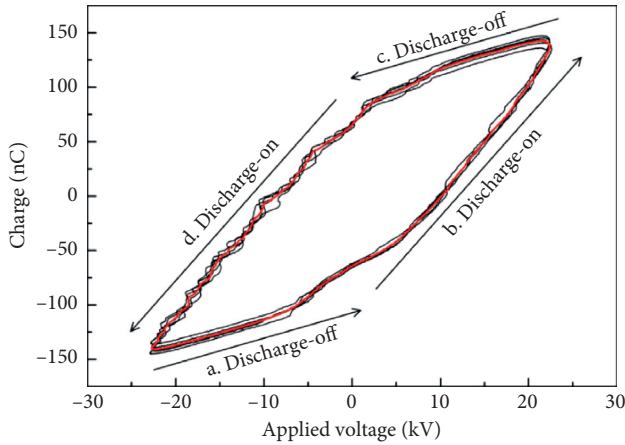


FIGURE 6: Typical presentation of Lissajous figure from sinusoidal voltage driven the coaxial DBD-PACA.

fluctuation of the power. As the excited particles and heat energy produced by the coaxial DBD-PACA discharge were blown away and given the presence of aerodynamic force, thus the microdischarge channels lengthened and the plasma temperature declined. Therefore, the applied voltage increased, and the quantity of the microdischarge channels rose and thus the power increased.

3.2. OES Characteristic

3.2.1. Emission Spectra of the Coaxial DBD-PACA. As a nonintrusive diagnostic method, the OES was widely used to diagnose plasma [33–37]; it can obtain important plasma data, such as the kinds and concentrations of excited particles, electron temperature, rotational temperature, and vibrational temperature. In this part, the integration time of the four channels of the spectrograph was set to 200 ms and the acquisition spectrum denoted the average of 20 cycles.

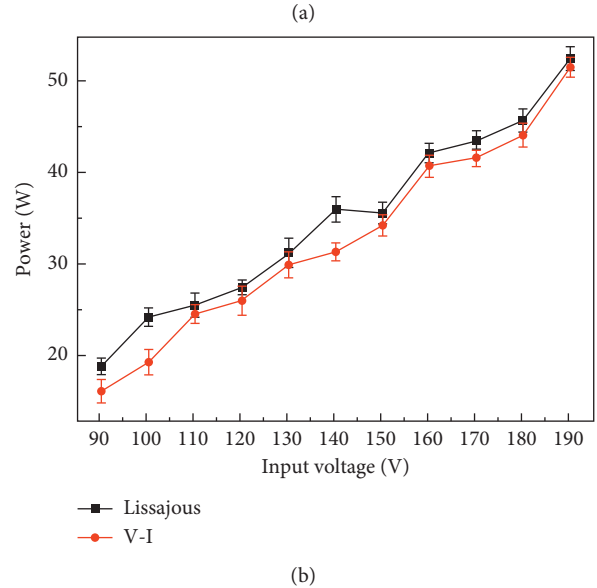
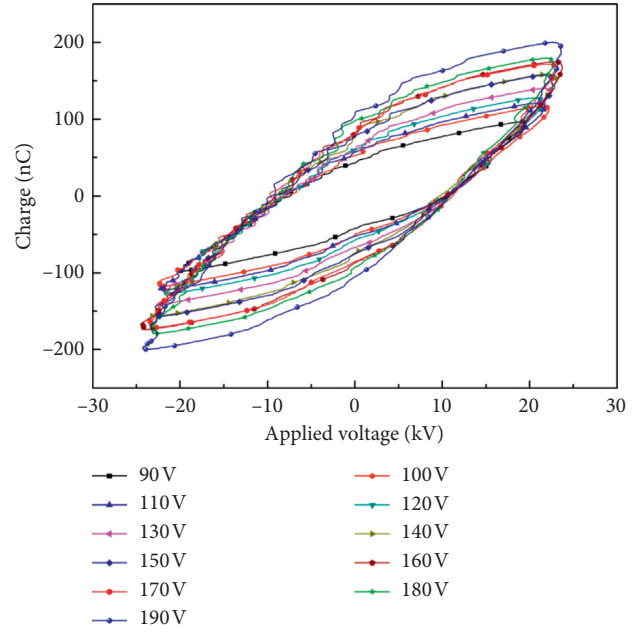


FIGURE 7: (a) Lissajous figures of the DBD-PACA under different input voltage and (b) the trend of power calculated by Lissajous figure and current-voltage methods with input voltage.

Figure 9 shows the typical coaxial DBD-PACA OES under the experimental conditions of 130 V input voltage and 200 L/min airflow rate. As depicted in Figure 9, the spectral lines were mainly composed of numerous nitrogen molecules SPS ($N_2(C^3\Pi_u \rightarrow B^3\Pi_g)$), several nitrogen ions first negative system (FNS, $N_2^+(B^2\Sigma_u^+ \rightarrow X^2\Sigma_u^+)$), and nitric oxide γ system ($NO(A^2\Sigma \rightarrow X^2\Pi)$). The SPS of nitrogen was produced by the $N_2(C^3\Pi_u)$ and $N_2(B^3\Pi_g)$ transitions, which was the strongest and most stable system in the emission spectrum of air. Since the ionization excitation potentials of $N_2(B^3\Pi_g)$ and $N_2(C^3\Pi_u)$ were 7.35 eV and 11.03 eV, respectively, as shown in equations (12) and (13), there were free electrons with energy higher than 11.03 eV in

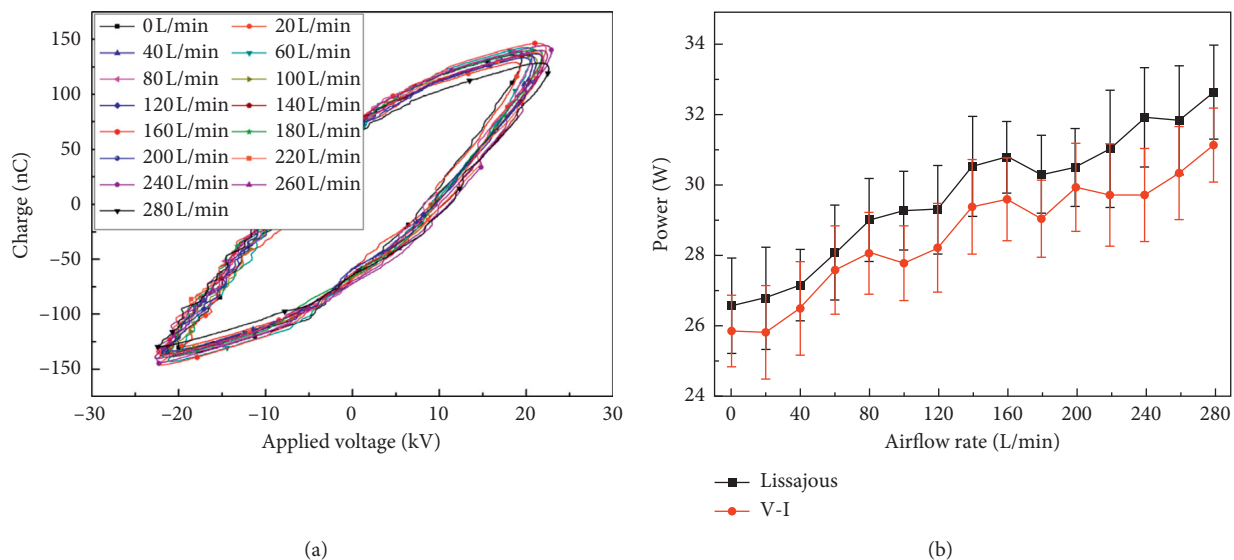


FIGURE 8: (a) Lissajous figures of the DBD-PACA under different airflow rate and (b) the trend of power calculated by Lissajous figure and current-voltage methods with airflow rate.

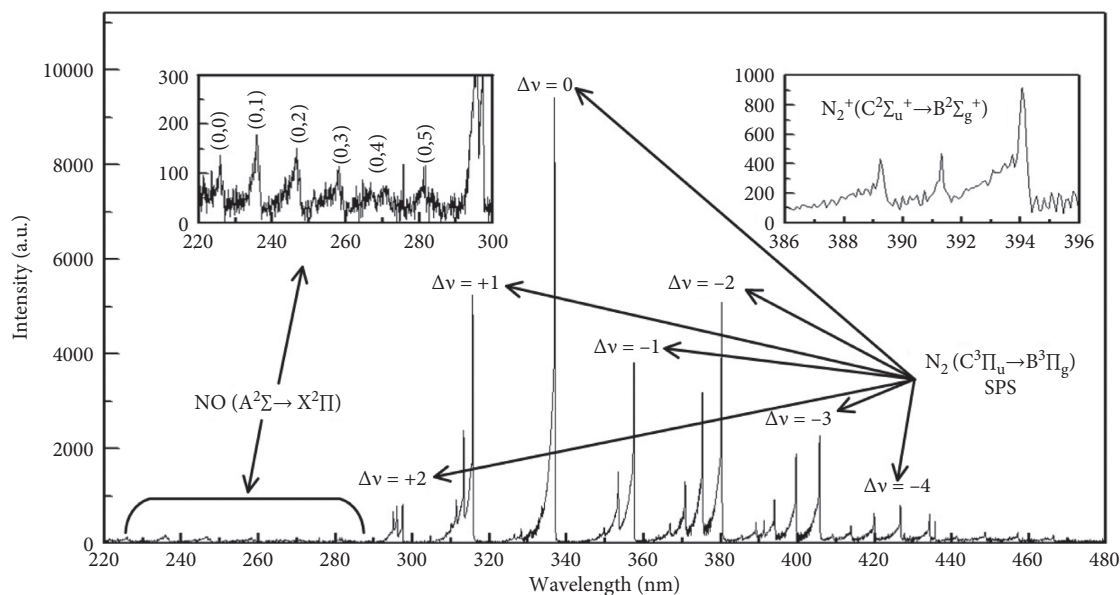
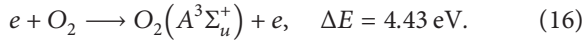
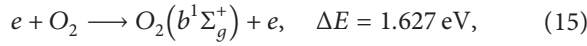
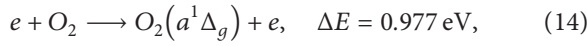
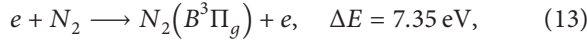
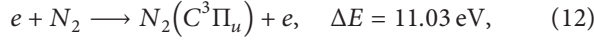


FIGURE 9: Typical coaxial DBD-PACA spectra at atmospheric pressure.

the plasma generated by the coaxial DBD-PACA discharge. As the excited nitrogen atoms had a short lifetime and fleetly recombined into nitrogen molecules, no spectral lines of excited nitrogen atoms were detected [38]. As ionization excitation potential of N_2^+ ($B^2\Sigma_u^+$) particle was as high as 18.76 eV and the energy level transition was mainly due to the collision of free electrons, thus the weak relative intensity of FNS spectral lines indicated that a notably low number of electrons exhibited an energy higher than 18.76 eV in the plasma. The most common excited particles in oxygen were O_2 ($a^1\Delta_g$), O_2 ($b^1\Sigma_g^+$), and O_2 ($A^3\Sigma_u^+$), whose excitation energies were

0.977 eV, 1.627 eV, and 4.43 eV, respectively, and can be produced by the collision between electrons and oxygen molecules, as shown in (14)–(16). These particles, however, have very low dissociation energies of 4.54 eV, 3.89 eV, and 1.15 eV, respectively, so they can easily collide with high-energy electrons to form ground state oxygen O (3P) and metastable oxygen O (1D), O (1S). Therefore, no oxygen molecules and atoms in the excited state were observed in the plasma generated by the coaxial DBD-PACA discharge. Next, the spectral lines of the SPS of nitrogen molecules with wavelength between 290 nm and 440 nm were studied.



In the experiment, the discharge plasma spectra were collected at ten points with equal spacing along the radial direction of the coaxial DBD-PACA, as shown in Figure 10. The spectral intensity along the radial direction varied obviously in the discharge area. As a whole, the intensity of the spectra increased in the direction away from the inner electrode. Next, the trends of the seven representative spectral lines (297.54 nm (2, 0), 315.76 nm (1, 0), 336.96 nm (0, 0), 357.56 nm (0, 1), 380.34 nm (0, 2), 405.80 nm (0, 3), 434.30 nm (0, 4)) of the SPS of nitrogen molecules were selected to study, as shown in Figure 11. As the radius increased, the intensity of spectral lines (297.54 nm, 315.76 nm, 336.96 nm, and 357.56 nm) first increased, then remained, and then increased rapidly and reached the maximum value at $r = 19$ mm. However, as the radius increased, the intensity of spectral lines (380.34 nm, 405.80 nm, and 434.30 nm) basically remained unchanged, then increased, and finally decreased and reached its maximum value at $r = 16$ mm. And the intensity of these three spectral lines almost disappeared at the position of $r = 19$ mm. In the SPS of nitrogen molecules, the spectral line intensity of the 336.96 nm was the strongest at almost all discharge regions of the coaxial DBD-PACA. This was mainly because the ground state was the easiest to obtain and the most abundant of all vibrational level states of the excited particles $N_2(C^3\Pi_u)$; meanwhile, the transitions between the ground state of $N_2(C^3\Pi_u)$ and $N_2(B^3\Pi_g)$ were the easiest transition path. However, the spectral line intensity of the 380.34 nm was the strongest at radiuses of 10 mm and 16 mm, respectively.

3.2.2. Effects of Input Voltage on Vibrational Temperature. The OES were collected at ten equidistant points in the radial direction of the coaxial DBD-PACA with different input voltages. And according to the multispectral line slope method mentioned above, when the airflow rate was 200 L/min, the vibrational temperatures at all collection points were calculated, as shown in Figure 12. It can be observed from Figure 12(a) that the vibrational temperature had the same tendency in the radial direction of the coaxial DBD-PACA when the input voltage changed, which first decreased quickly and then increased, and reached the minimum at $r = 18$ mm. Figure 12(b) shows that the vibrational temperature at each collection point reduced but slightly fluctuated, with the increase of the input voltage. It was found that vibrational excitation dominated the input energy coupling when the reduced electric field was small, while electronic excitation dominated when the reduced

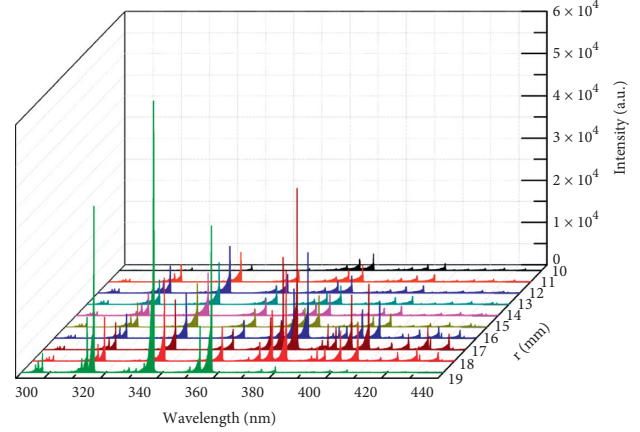


FIGURE 10: The spectral distribution trend of ten collection points in the radial direction, when the input voltage was 130 V and the air flow was 200 L/min.

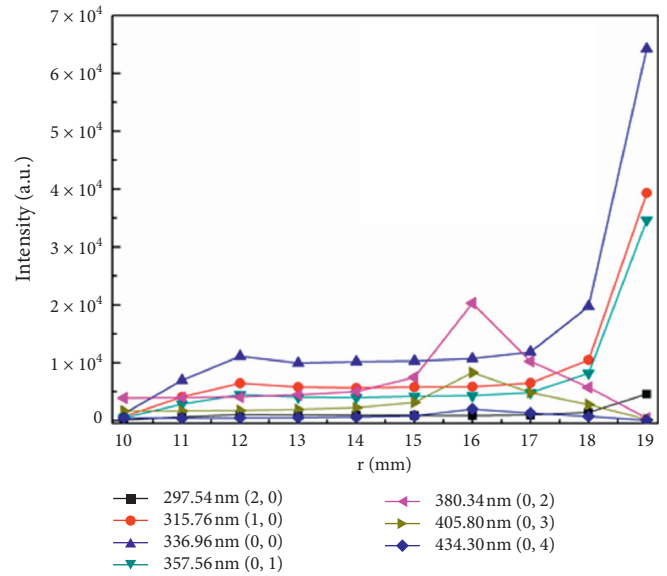


FIGURE 11: The trends of seven representative spectral lines of the SPS of the nitrogen molecules.

electric field was great by solving the Boltzmann equation [39]. And when the coaxial DBD-PACA driven by a single-high-voltage power supply discharged, the closer to the inner electrode connected to the ground, the smaller the reduced electric field; and the closer to the outer electrode connected to the high voltage, the greater the reduced electric field [40]. Thereby the vibrational temperature decreased with the increase of the input voltage.

3.2.3. Effects of Airflow Rate on Vibrational Temperature. The OES were collected at ten equidistant points in the radial direction of the coaxial DBD-PACA at different airflow rates. And Figure 13 shows the vibrational temperature at all collection positions at the condition of the input voltage being 130 V. As the radius increased, the vibrational temperature first decreased and then increased

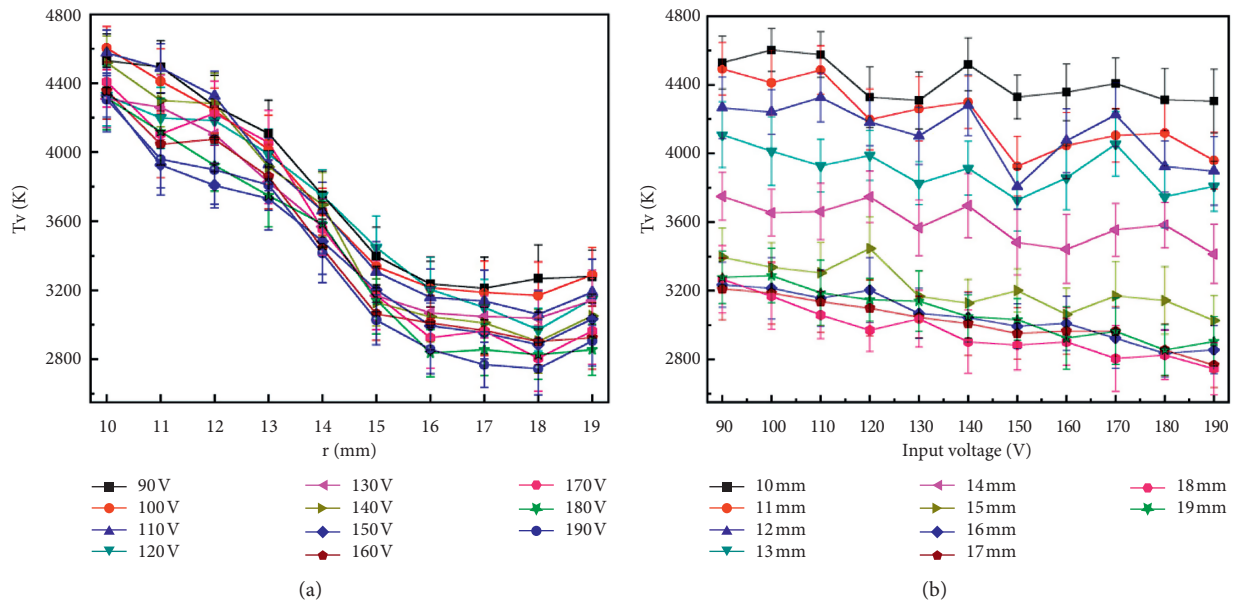


FIGURE 12: (a) Vibrational temperature varied with the radius of the coaxial DBD-PACA at different input voltage; (b) vibrational temperature varied with the input voltage at different points.

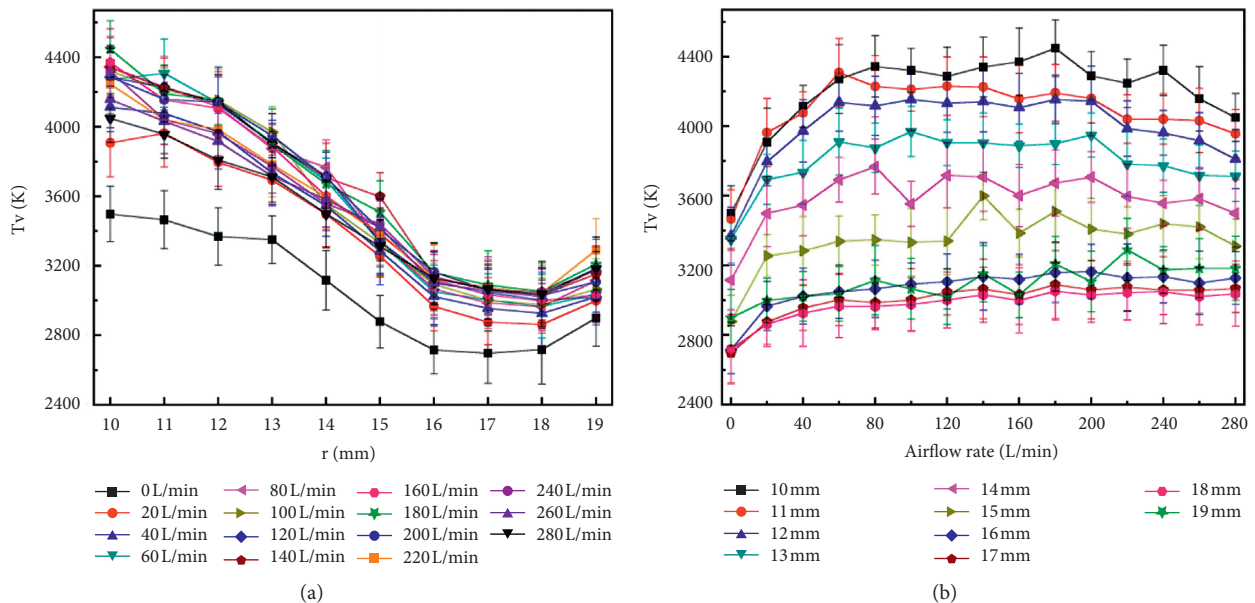


FIGURE 13: (a) Vibrational temperature varied with the radius of the coaxial DBD-PACA at different airflow rate; (b) vibrational temperature varied with the airflow rate at different points.

and reached the minimum value at $r = 18$ mm, as shown in Figure 13(a). As we can see from Figure 13(b), within the range of 0–280 L/min, when r was less than 15 mm, the vibrational temperature first increased rapidly and then decreased slowly; when r was greater than 15 mm, the vibrational temperature first increased and then basically remained stable. As the discharge was nonuniform in still air, the vibrational temperature reduced obviously when the airflow rate was 0 L/min. The smaller the radius was, the more the vibrational temperature was influenced by the airflow rate.

4. Conclusions

In this paper, a coaxial DBD-PACA system was established to study its discharge and OES characteristics. Lissajous figure method and current-voltage method were used to calculate the power consumption of the coaxial DBD-PACA. And the vibrational temperature was obtained by means of fitting spectral intensity of nitrogen molecule SPS; meanwhile, the influences of input voltage and airflow rate on vibrational temperature were studied. The main conclusions were as follows.

It was found that the breakdown input voltage and extinction input voltage both increased with increasing airflow rate, and breakdown input voltage was notably greater than extinction input voltage. The coaxial DBD-PACA only discharged in the stages b and d, and the discharge became more intense in stage d. The powers measured by Lissajous figure method and current-voltage method were similar, and the power increased with increasing input voltage and airflow rate.

A number of SPS excited nitrogen molecules were detected in the discharge plasma. And the trends of seven representative spectral intensities of the SPS nitrogen molecules were different in different discharge region. Meanwhile, the vibrational temperature varied significantly in different discharge region. The vibrational temperature decreased with the increase of the input voltage; however, the vibrational temperature first increased, then remained, and lastly decreased with the increase of the airflow rate.

Furthermore, the results obtained revealed the performance of the coaxial DBD-PACA. However, the ultimate goal is to install the coaxial DBD-PACA on the aero-engine to assist combustion. Therefore, the coaxial DBD-PACA will be installed on the combustion chamber to study the influence of the coaxial DBD-PACA on combustion in the future.

Data Availability

The data used to support the findings of this study are included within the article.

Conflicts of Interest

The authors declare that there are no conflicts of interest regarding the publication of this paper.

Acknowledgments

This research was funded by the Key Project of National Natural Science Foundation of China (Grant no. 51436008) and the Youths Science Foundation Project of National Natural Science Foundation of China (Grant no. 51806245).

References

- [1] W. Crookes, "On radiant matter, lecture delivered before the British association for the advancement of science," *American Journal of Science*, vol. 18, no. 3, pp. 241–262, 1879.
- [2] L. Tonks and I. Langmuir, "Oscillations in ionized gases," *Physical Review*, vol. 33, no. 2, pp. 195–210, 1929.
- [3] A. Starikovskiy and N. Aleksandrov, "Plasma-assisted ignition and combustion," *Progress in Energy and Combustion Science*, vol. 39, no. 1, pp. 61–110, 2013.
- [4] D. Azar, J. T. Lott, E. Jabbarzadeh, T. Shazly, and V. B. Kolachalama, "Surface modification using ultraviolet-ozone treatment enhances acute drug transfer in drug-coated balloon therapy," *Langmuir*, vol. 36, no. 17, pp. 4645–4653, 2020.
- [5] N. Hayashi, M. Goto, T. Itarashiki, A. Yonesu, and A. Sakudo, "Current plasma sterilization and disinfection studies," *Journal of Photopolymer Science and Technology*, vol. 31, no. 3, pp. 389–398, 2018.
- [6] S. C. Ji, B. Zhang, J. Li et al., "Numerical study for active flow control using dielectric barrier discharge actuators," *Journal of Aerospace Engineering*, vol. 30, no. 5, Article ID 04017050, 2017.
- [7] F. Gui, H. Wang, P. Wang et al., "The mutation breeding and mutagenic effect of air plasma on *Penicillium chrysogenum*," *Plasma Science and Technology*, vol. 14, no. 4, pp. 297–302, 2012.
- [8] H. Joonsik, B. Choongsik, P. Jooyoung et al., "Microwave-assisted plasma ignition in a constant volume combustion chamber," *Combustion and Flame*, vol. 167, pp. 86–96, 2016.
- [9] J. V. Pastor, J. M. García-Oliver, A. García, and M. Pinotti, "Effect of laser induced plasma ignition timing and location on diesel spray combustion," *Energy Conversion and Management*, vol. 133, pp. 41–55, 2017.
- [10] J. C. Sagás, H. S. Maciel, and P. T. Lacava, "Effects of non-steady state discharge plasma on natural gas combustion: flammability limits, flame behavior and hydrogen production," *Fuel*, vol. 182, pp. 118–123, 2016.
- [11] V. R. Axel, L. Serge, M. Philippe et al., "Plasma assisted combustion: effect of a coaxial DBD on a methane diffusion flame," *Plasma Sources Science and Technology*, vol. 16, no. 1, pp. 149–160, 2007.
- [12] J. C. Sagás, A. H. Neto, A. C. Pereira Filho, H. S. Maciel, and P. T. Lacava, "Basic characteristics of gliding-arc discharges in air and natural gas," *IEEE Transactions on Plasma Science*, vol. 39, no. 2, pp. 775–780, 2011.
- [13] G. Vanhove, M.-A. Boumejdi, S. Shcherbanev, Y. Fenard, P. Desgroux, and S. M. Starikovskaia, "A comparative experimental kinetic study of spontaneous and plasma-assisted cool flames in a rapid compression machine," *Proceedings of the Combustion Institute*, vol. 36, no. 3, pp. 4137–4143, 2017.
- [14] K. Togai, N. Tsolas, and R. A. Yetter, "Kinetic modeling and sensitivity analysis of plasma-assisted oxidation in a $H_2/O_2/Ar$ mixture," *Combustion and Flame*, vol. 164, pp. 239–249, 2016.
- [15] Y. Pang, T. Hammer, D. Müller et al., "Investigation of non-thermal plasma assisted charcoal gasification for production of hydrogen-rich syngas," *Processes*, vol. 7, no. 2, Article ID 7020114, 114 pages, 2019.
- [16] I. B. Matveev and L. A. Rosocha, "Guest editorial classification of plasma systems for plasma-assisted combustion," *IEEE Transactions on Plasma Science*, vol. 38, no. 12, pp. 3257–3264, 2010.
- [17] C. A. Fuh and C. Wang, "A novel combustion platform for microwave plasma-assisted combustion studies," *IEEE Transactions on Plasma Science*, vol. 46, no. 5, pp. 1800–1808, 2018.
- [18] W. Kim, H. Do, M. G. Mungal et al., "Flame stabilization enhancement and NO_x production using ultra short repetitively pulsed plasma discharges," in *Proceeding of the 44th AIAA Aerospace Sciences Meeting and Exhibit*, Reno NV, USA, January 2006.
- [19] J. E. Retter, R. A. Fontaine, J. B. Freund et al., "Coaxial DBD actuator design for control of a hydrogen diffusion flame," in *Proceedings of the 54th AIAA Aerospace Science Meeting*, San Diego, CA, USA, January 2016.
- [20] E. I. Mintoussov, E. M. Anokhin, and A. Y. Starikovskii, "Plasma assisted combustion and fuel reforming," in *Proceedings of the 45th AIAA Aerospace Science Meeting and Exhibit*, Reno, NV, USA, January 2007.
- [21] J.-F. Tang, D.-S. Zhou, M. Tang, X.-M. Zhu, and C.-H. Zhang, "Experimental investigation on a multicathode dielectric-

- barrier discharge: effects of airflows,” *IEEE Transactions on Plasma Science*, vol. 47, no. 5, pp. 1944–1949, 2019.
- [22] Y. Ju and W. Sun, “Plasma assisted combustion: dynamics and chemistry,” *Progress in Energy and Combustion Science*, vol. 48, pp. 21–83, 2015.
- [23] Z. He, Z. H. Liang, X. N. Zhang et al., “Influence of copper nanowires grown in a dielectric layer on the performance of dielectric barrier discharge,” *Journal of Vacuum Science and Technology B*, vol. 35, no. 1, Article ID 010603, 2017.
- [24] B. Lin, Y. Wu, Y. Zhu, F. Song, and D. Bian, “Experimental investigation of gliding arc plasma fuel injector for ignition and extinction performance improvement,” *Applied Energy*, vol. 235, pp. 1017–1026, 2019.
- [25] H. Jiang, T. Shao, C. Zhang et al., “Experimental study of Q-V Lissajous figures in nanosecond-pulse surface discharges,” *IEEE Transactions on Dielectrics and Electrical Insulation*, vol. 20, no. 4, pp. 1101–1111, 2013.
- [26] T. C. Manley, “The electric characteristics of the ozonator discharge,” *Transactions of the Electrochemical Society*, vol. 84, no. 1, pp. 83–96, 1943.
- [27] D. E. Ashpis, M. C. Laun, and E. L. Griebeler, “Progress toward accurate measurement of dielectric barrier discharge plasma actuator power,” *AIAA Journal*, vol. 55, no. 7, pp. 2254–2268, 2017.
- [28] S. Acquaviva, “Simulation of emission molecular spectra by a semi-automatic programme package: the case of C₂ and CN diatomic molecules emitting during laser ablation of a graphite target in nitrogen environment,” *Spectrochimica Acta Part A: Molecular and Biomolecular Spectroscopy*, vol. 60, no. 8-9, pp. 2079–2086, 2004.
- [29] D. E. Shemansky and A. L. Broadfoot, “Excitation of N₂ and N + 2 systems by electrons-I. Absolute transition probabilities,” *Journal of Quantitative Spectroscopy and Radiative Transfer*, vol. 11, no. 10, pp. 1385–1400, 1971.
- [30] I. Moralev, V. Sherbakova, I. Selivonin, V. Bityurin, and M. Ustinov, “Effect of the discharge constriction in DBD plasma actuator on the laminar boundary layer,” *International Journal of Heat and Mass Transfer*, vol. 116, pp. 1326–1340, 2018.
- [31] J. H. Lee, S. Y. Jeong, G. Kim et al., “Reinforcing the built-in field for efficient charge collection in polymer solar cells,” *Advanced Functional Materials*, vol. 28, no. 10, Article ID 1705079, 2018.
- [32] C. W. Yao, S. Chen, S. Wang et al., “Characteristics of atmospheric Ar/NH₃ DBD and its comparison with He/N₂ DBD,” *Journal of Physics D: Applied Physics*, vol. 51, no. 22, Article ID 225201, 2018.
- [33] I. V. Adamovich and W. R. Lempert, “Challenges in understanding and predictive model development of plasma-assisted combustion,” *Plasma Physics Controlled Fusion*, vol. 57, no. 1, Article ID 014001, 2014.
- [34] D. C. Boyer, S. Mouda, O. Gueguen et al., “Determination of iodine in polyamide by inductively-coupled plasma/mass spectrometry,” *Talanta*, vol. 189, pp. 568–572, 2018.
- [35] Z. D. Kang and Y. K. Pu, “Molecular nitrogen vibrational temperature in an inductively coupled plasma,” *Chinese Physics Letters*, vol. 19, no. 2, pp. 211–213, 2002.
- [36] Y. Wu, Y. H. Li, M. Jia et al., “Experimental investigation into characteristics of plasma aerodynamic actuation generated by dielectric barrier discharge,” *Chinese Journal of Aeronautics*, vol. 23, no. 1, pp. 39–45, 2010.
- [37] S. Tada, S. Takashima, M. Ito, M. Hori, T. Goto, and Y. Sakamoto, “Measurement and control of absolute nitrogen atom density in an electron-beam-excited plasma using vacuum ultraviolet absorption spectroscopy,” *Journal of Applied Physics*, vol. 88, no. 4, pp. 1756–1759, 2000.
- [38] S. Yang, S. Nagaraja, W. T. Sun et al., “Multi-scale modeling and general theory of non-equilibrium plasma-assisted ignition and combustion,” *Journal of Physics D: Applied Physics*, vol. 50, no. 43, Article ID 433001, 2017.
- [39] S. Nagaraja, V. Yang, and I. Adamovich, “Multi-scale modelling of pulsed nanosecond dielectric barrier plasma discharges in plane-to-plane geometry,” *Journal of Physics D: Applied Physics*, vol. 46, no. 13, Article ID 155205, 2013.
- [40] C. R. Miao, F. Liu, Q. Wang et al., “Investigation on the influence of electrode geometry on characteristics of coaxial dielectric barrier discharge reactor driven by an oscillating microsecond pulsed power supply,” *The European Physical Journal D*, vol. 72, no. 3, 2018.